JOURNAL OF SPACECRAFT AND ROCKETS
Vol. 38, No. 2, March–April 2001

Lateral–Directional Coupling and Unsteady Aerodynamic Effects of Hypersonic Vehicles

Christian Breitsamter,* Tomislav Cvrlje,† Boris Laschka,‡ Matthias Heller,§ and Gottfried Sachs¶
Technical University of Munich, 85747 Garching, Germany

Results from a joint research program of the Institutes of Fluid Dynamics and of Flight Mechanics and Flight Control of the Technical University of Munich on a two-stage space transportation system are presented. The unsteady aerodynamics resulting from an orbital stage at stage separation flow conditions at Mach number 6.8 are first discussed. Unsteady flowfields associated with yaw and roll oscillations of the orbital stage at a certain distance above the carrier stage are investigated. The calculations are based on a finite volume method for real-time solutions of the unsteady Euler equations. The results focus on pressure distributions and aerodynamic coefficients providing an essential means for carrying out stability and control investigations. In the second part, flight mechanics stability and control problems are addressed considering key issues of lateral–directional dynamics. Inherent vehicle characteristics can show specific stability and flying quality deficiencies in hypersonic flight, concerning a partially unstable dutch roll mode with high roll–yaw coupling and weak roll damping. There is also a coupling of the roll and spiral poles for certain configurations, yielding a slow, eventually unstable oscillation called lateral phugoid. Reasons and effects for the stability deficiencies are discussed, including conditions of existence for the lateral phugoid.

Nomenclature

$\boldsymbol{A}, \boldsymbol{E}$	=	system and disturbance matrices
$\boldsymbol{B}$	=	control effectiveness matrix
$\boldsymbol{C}, \boldsymbol{D}$	=	output and direct feed matrices
C_l	=	roll moment coefficient, roll moment$/q_\infty S s_{\text{ref}}$
C_{lp}	=	$[\partial C_l/\partial(p s_{\text{ref}}/2V_0)]$, per rad
C_{lr}	=	$[\partial C_l/\partial(r s_{\text{ref}}/2V_0)]$, per rad
$C_{l\beta}$	=	$(\partial C_l/\partial\beta)$, per deg or rad
$C_{l\zeta}$	=	$(\partial C_l/\partial\zeta)$, per deg or rad
$C_{l\xi}$	=	$(\partial C_l/\partial\xi)$, per deg or rad
C_n	=	yaw moment coefficient, yaw moment$/q_\infty S s_{\text{ref}}$
C_{np}	=	$[\partial C_n/\partial(p s_{\text{ref}}/2V_0)]$, per rad
C_{nr}	=	$[\partial C_n/\partial(r s_{\text{ref}}/2V_0)]$, per rad
$C_{n\beta}$	=	$(\partial C_n/\partial\beta)$, per deg or rad
$C_{n\zeta}$	=	$(\partial C_n/\partial\zeta)$, per deg or rad
$C_{n\xi}$	=	$(\partial C_n/\partial\xi)$, per deg or rad
C_Y	=	side force coefficient, side force$/q_\infty S$
C_{Yp}	=	$[\partial C_Y/\partial(p s_{\text{ref}}/2V_0)]$, per rad
C_{Yr}	=	$[\partial C_Y/\partial(r s_{\text{ref}}/2V_0)]$, per rad
$C_{Y\beta}$	=	$(\partial C_Y/\partial\beta)$, per deg or rad
$C_{Y\zeta}$	=	$(\partial C_Y/\partial\zeta)$, per deg or rad
$C_{Y\xi}$	=	$(\partial C_Y/\partial\xi)$, per deg or rad
f	=	frequency of oscillation, Hz
g	=	acceleration due to gravity, m/s^2
h	=	vertical distance between the carrier stage upper surface (flat plate) and the orbital stage reference point x_M (Fig. 1), m
I_x, I_z, I_{xz}	=	moments of inertia with respect to Cartesian coordinates, kgm^2
I_Δ	=	$I_x I_z - I_{xz}^2$, kg^{2}m^4
k	=	reduced frequency, $L\omega\sqrt{(\rho_\infty/p_\infty)}/[M_\infty\sqrt{(\gamma)}]$
L	=	orbital stage reference length, m
L_p	=	dimensional roll stability derivative due to roll rate, $[q_0 S s_{\text{ref}}^2/(2V_0 I_\Delta)](I_z C_{lp} + I_{xz} C_{np})$, 1/s
L_r	=	dimensional roll stability derivative due to yaw rate, $[q_0 S s_{\text{ref}}^2/(2V_0 I_\Delta)](I_z C_{lr} + I_{xz} C_{nr})$, 1/s
L_β	=	dimensional roll stability derivative due to sideslip, $(q_0 S s_{\text{ref}}/I_\Delta)(I_z C_{l\beta} + I_{xz} C_{n\beta})$, 1/s^2
L_ζ	=	dimensional roll stability derivative due to rudder deflection, $(q_0 S s_{\text{ref}}/I_\Delta)(I_z C_{l\zeta} + I_{xz} C_{n\zeta})$, 1/s^2
L_ξ	=	dimensional roll stability derivative due to taileron deflection, $(q_0 S s_{\text{ref}}/I_\Delta)(I_z C_{l\xi} + I_{xz} C_{n\xi})$, 1/s^2
l_{ref}	=	reference chord, m
M	=	Mach number
m	=	mass of vehicle, kg
N_p	=	dimensional yaw stability derivative due to roll rate, $[q_0 S s_{\text{ref}}^2/(2V_0 I_\Delta)](I_x C_{np} + I_{xz} C_{lp})$, 1/s
N_r	=	dimensional yaw stability derivative due to yaw rate, $[q_0 S s_{\text{ref}}^2/(2V_0 I_\Delta)](I_x C_{nr} + I_{xz} C_{lr})$, 1/s
N_β	=	dimensional yaw stability derivative due to sideslip, $(q_0 S s_{\text{ref}}/I_\Delta)(I_x C_{n\beta} + I_{xz} C_{l\beta})$, 1/s^2
N_ζ	=	dimensional yaw stability derivative due to rudder deflection, $(q_0 S s_{\text{ref}}/I_\Delta)(I_x C_{n\zeta} + I_{xz} C_{l\zeta})$, 1/s^2
N_ξ	=	dimensional yaw stability derivative due to taileron deflection, $(q_0 S s_{\text{ref}}/I_\Delta)(I_x C_{n\xi} + I_{xz} C_{l\xi})$, 1/s^2
p	=	pressure, N/m^2
p, q, r	=	roll, pitch, and yaw rate (angular velocities), rad/s
q	=	dynamic pressure, N/m^2
S	=	reference area, m^2
s	=	Laplace operator
s_{ref}	=	reference half-span, (orbital stage $:= L$), m
T_D	=	time to double, s
T_R	=	roll time constant, s
t	=	time, s
u, v, w	=	axial, lateral, and vertical velocities, m/s
$\boldsymbol{u}$	=	control input vector
V	=	freestream velocity, m/s
x, y, z	=	Cartesian coordinates, m
$\boldsymbol{x}, \boldsymbol{y}, \boldsymbol{z}$	=	state, output, and disturbance vectors
x_D	=	orbital stage maximum thickness position, m
x_M	=	moment reference position of orbital stage, m
x_V, y_N	=	orbital stage forebody length and width, respectively, m

Presented as Paper 99-4832 at the 9th International Space Planes and Hypersonic Systems and Technologies Conference, Norfolk, VA, 1–5 November 1999; received 5 January 2000; revision received 10 November 2000; accepted for publication 16 November 2000.

*Chief Scientist, Lehrstuhl für Fluidmechanik. Member AIAA.
†Research Engineer, Lehrstuhl für Fluidmechanik. Member AIAA.
‡Chair, Lehrstuhl für Fluidmechanik. Honorary Fellow AIAA.
§Scientific Engineer, Lehrstuhl für Flugmechanik und Flugregelung. Member AIAA.
¶Chair, Lehrstuhl für Flugmechanik und Flugregelung. Fellow AIAA.

x_{for}, x_{ref}, x_{opt} = forward, reference, and optimum axial positions of center of gravity, m
Y_p = dimensional sideslip stability derivative due to roll rate, $[q_0 S s_{ref}/(2V_0^2 m)]C_{yp}$
Y_r = dimensional sideslip stability derivative due to yaw rate, $[q_0 S s_{ref}/(2V_0^2 m)]C_{yr}$
Y_β = dimensional sideslip stability derivative due to sideslip, $q_0 S/(V_0 m)C_{y\beta}$
Y_ζ = dimensional sideslip stability derivative due to rudder deflection, $q_0 S/(V_0 m)C_{y\zeta}$, 1/s
Y_ξ = dimensional sideslip stability derivative due to taileron deflection, $q_0 S/(V_0 m)C_{y\xi}$, 1/s
α = angle of attack, deg or rad
β = angle of sideslip, deg or rad
β_0 = mean angle of yaw oscillation, deg or rad
γ = ratio of specific heat; flight-path angle, deg or rad
$\Delta\beta$ = amplitude of yaw oscillation, deg or rad
$\Delta\Phi$ = amplitude of roll oscillation, deg or rad
ζ = rudder deflection, deg or rad; damping coefficient
θ = pitch angle, deg or rad
ξ = taileron deflection, deg or rad
ρ = density, kg/m^3
σ = real part of eigenvalue
τ = dimensionless time, $Ma_\infty\sqrt{(\gamma)}t\sqrt{(p_\infty/\rho_\infty)}/L$
Φ = angle of bank, deg or rad
Φ_F, Φ_V = orbital stage wing and forebody sweep, respectively, deg
Φ_0 = mean angle of roll oscillation, deg or rad
Ψ = heading angle, deg or rad
ω = angular frequency, $2\pi f$, Hz
ω_n = natural frequency, Hz

Subscripts

cg = center of gravity
crit = critical
K = inertial
max, min = maximum, minimum
W = wind
0 = reference condition
∞ = freestream values

Introduction

CURRENTLY, there is considerable effort in the field of hypersonic research to establish a technology base for innovative, fully reusable space transportation systems.[1–5] In the last few years, significant progress in the research of hypersonic flight and the development of demonstrators has been achieved, for example, by the NASA Hyper-X Program and the X-33 Reusable Launch Vehicle Demonstrator Program.[6] However, there are still challenging problems in many technological areas, and hence, a significant need for fundamental hypersonic research exists.

Detailed investigations concerning key technologies for a two-stage space transportation system are being performed in the Collaborative Research Center 255 Transatmospheric Flight Systems of the Deutsche Forschungsgemeinschaft at the Technical University of Munich. When the separation maneuver of such a two-staged system is considered, there are three flight phases, each of which shows specific characteristics. In the first phase, where the flight system performs a pull-up maneuver, the orbital stage is placed into a position at high altitude (35 km) to be released from the carrier stage at high Mach number ($M_\infty = 6.8$). When the orbital stage is released, the second phase starts focusing on the separation of the orbital stage from the carrier stage. The stage separation is highly dominated by aerodynamic interference effects. Safety considerations are of great interest to achieve a certain distance between the two vehicles as fast as possible. Appropriate control techniques are required to perform an optimum separation maneuver to avoid critical flight situations. The third phase refers to the stand-alone flight of both vehicles without any interaction of the stages. Regarding the separation phase, there may be significant problems in the fields of aerothermodynamics,[7] as well as of flight mechanics stability and control.

Extensive numerical simulations have demonstrated that during the separation phase, strong reflecting shock waves occur between the orbital and the carrier stages.[8,9] The propagation of the shock waves depends on the separation speed, the distance between the two stages, and the incidence of the stages. Thus, the points of intersection of the shock waves change significantly, which causes strong, unsteady airloads on the orbital stage. Commonly, the stage separation is treated as a pure longitudinal motion, but small disturbances may also evoke some superimposed lateral motions. The unsteady aerodynamic forces and moments induced by such lateral–directional motions must be analyzed in detail to assess stability and control properties. The calculations of the unsteady flowfields are based on the solution of the unsteady Euler equations. Their application provides a reasonable means to describe the shock wave systems between both stages, as well as the body wakes, and to determine force and moment coefficients of the separating body.[10] When only small angles of attack, as well as small angles of sideslip and bank, are considered, it is assumed that flow separation due to friction does not predominate the flowfield characteristics.

Furthermore, the unique aerodynamic and propulsion configuration of hypersonic vehicles causes specific flight mechanics effects that are not existent with aircraft of conventional speed range. Particular problems related to flight in the high Mach number regime are concerned with inherent stability and control deficiencies including instabilities, specific damping as well as coupling characteristics, and decreasing effectiveness of the aerodynamic control surfaces with Mach number.[11,12] These effects are of special concern for lateral dynamics because here considerable coupling of the related modes of motions exists. Therefore, research in the field of hypersonic lateral dynamics and stability and control is required.

Orbital Stage Lateral Unsteady Aerodynamics

Computational Fluid Dynamics

The numerical simulation is based on a finite volume approximation to the integral form of the unsteady Euler equations using explicit time integration. The time-dependent flow vector for multidimensional problems is calculated by using the Strang-type of fractional step. The numerical fluxes are calculated by the modified advection upstream splitting method (AUSM).[13,14] This method was employed because it has proved to be very stable for hypersonic applications. In particular, in the wake region of the orbital stage, the previously used total variation diminishing–flux difference Splitting scheme employing Roe-averaged weighted quantities at the cell interfaces shows notable disadvantages. The modified AUSM scheme represents a hybrid approach between the van Leer flux vector splitting scheme and the original AUSM scheme.[15] The AUSM scheme is based on the idea of regarding the convection and acoustic waves as physically distinct processes and, thus, defining the fluxes as a sum of the convective and pressure terms.[16] To guarantee high-order accuracy in the spatial domain, the left and right states at the cell interfaces are obtained with the MUSCL approach. The van Albada limiter function is chosen to extrapolate the state values and, thus, provides high-order fluxes in smooth regions. At discontinuities, the function switches to first-order accuracy to ensure optimal shock-capturing features.[13]

Impermeable wall characteristic boundary conditions are applied to evaluate the primitive variables. At the farfield boundaries, the flow variables are set to their freestream values for hypersonic inflow conditions; whereas for outflow conditions, the flow variables are extrapolated by employing the solution of the computational domain.

Geometry and Grid Generation

The unsteady calculations are conducted for the configuration of a generic orbital stage at stage separation flow conditions. To consider shock interference of the carrier stage on the orbital stage and to achieve high numerical efficiency in the simulations, the computational domain includes only the carrier stage upper surface represented by a flat plate in the region of the orbital stage. A side and top view of the orbital stage displaying all relevant geometric quantities are shown in Fig. 1. The middle section of the orbital stage consists

of two partial ellipses, a mainly flat lower side and a flat tail section. The surface of the body is described from a discrete set of points provided by an algebraic grid generator.

The computational mesh is created by a Poisson algorithm based on a multiblock grid of nine blocks arranged in hybrid C–H topology[17,18] (Fig. 2). The overall mesh consists of 140,000 cells. The surface of the body involves 6500 cells. The block boundaries are emphasized by bold lines in Fig. 2. Elliptic smoothing is applied for each block and, in the same manner, over block boundaries. The connections between adjacent blocks are organized by mother–child relations where the grid points located at block connections are allowed to move during the iteration process.[17,18] The convergence criterion for sufficient smoothness is fulfilled if the change in the source strengths is below 10^{-5}. For unsteady calculations, the grid is dynamically adapted to the actual body position. The separating body is moved for each time step according to the prescribed motion. Because of the motion-induced mesh deformations near the body, it is necessary to smooth the grid again using the Poisson algorithm. The unsteady transformation of the Euler equations takes into account the velocity of the mesh, as well as the deformation of the cells.

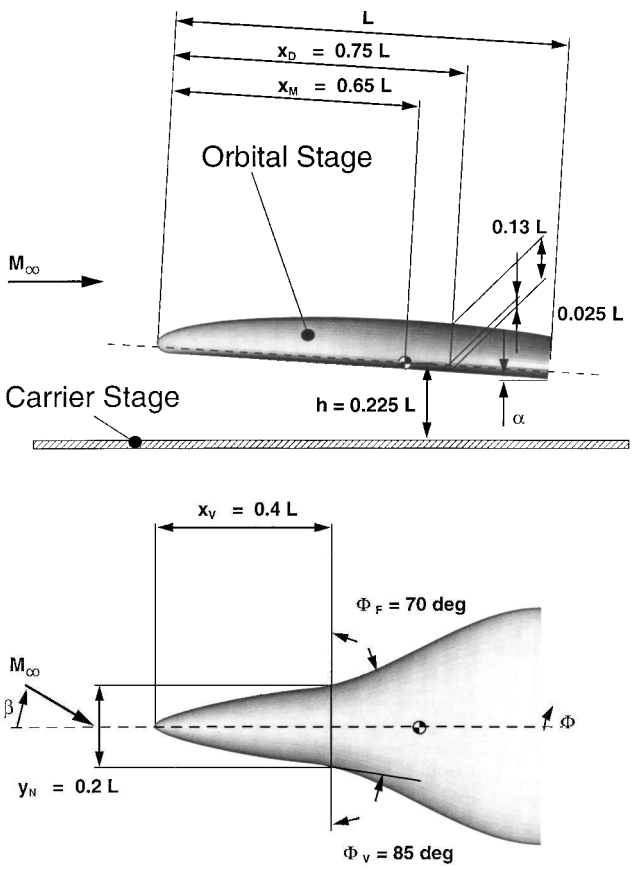

Fig. 1 Geometry of the generic orbital stage.

Numerical Accuracy

The accuracy of the Euler code has been proved by evaluating several standard test cases for subsonic, supersonic, and hypersonic flow.[14,17,18] In addition, grid convergence studies are carried out for steady cases using a refined grid of 900,000 cells with the orbital stage at fixed positions above the carrier stage.[14] The steady-state calculations substantiate that the dominant flow features are represented correctly by the standard grid resolution of 140,000 cells related to the results shown herein.

Computational Results and Analysis

The orbital stage harmonic motions are performed at an initial position of the orbital stage relative to the carrier stage. This initial position is defined by a vertical distance of $h/L = 0.225$ between the carrier stage upper surface (flat plate) and the orbital stage moment reference point at $x_M/L = 0.65$ (Fig. 1). The freestream conditions refer to a Mach number of $M_\infty = 6.8$ and an orbital stage angle of attack of $\alpha = 0$ deg. The freestream conditions are held constant for all numerical simulations presented. The orbital stage reference length L is used to evaluate the lateral–directional moment coefficients, C_l and C_n. The convergence criterion of the steady-state solution of the Euler equations is reached if the residual of the density does not exceed 10^{-6}. When starting from the steady solution of the initial state,[14,17] the orbital stage performs harmonic yaw oscillations described by

$$\beta(\tau) = \beta_0 + \Delta\beta \sin(k\tau) \tag{1}$$

and harmonic roll oscillations described by

$$\Phi(\tau) = \Phi_0 + \Delta\Phi \sin(k\tau) \tag{2}$$

Reduced frequencies of $k = 0.1$ and $k = 0.5$ are used to study the influence and magnitude of unsteady effects. Both the yaw and roll oscillations of the orbital stage are carried out at $\beta_0 = 0$ deg

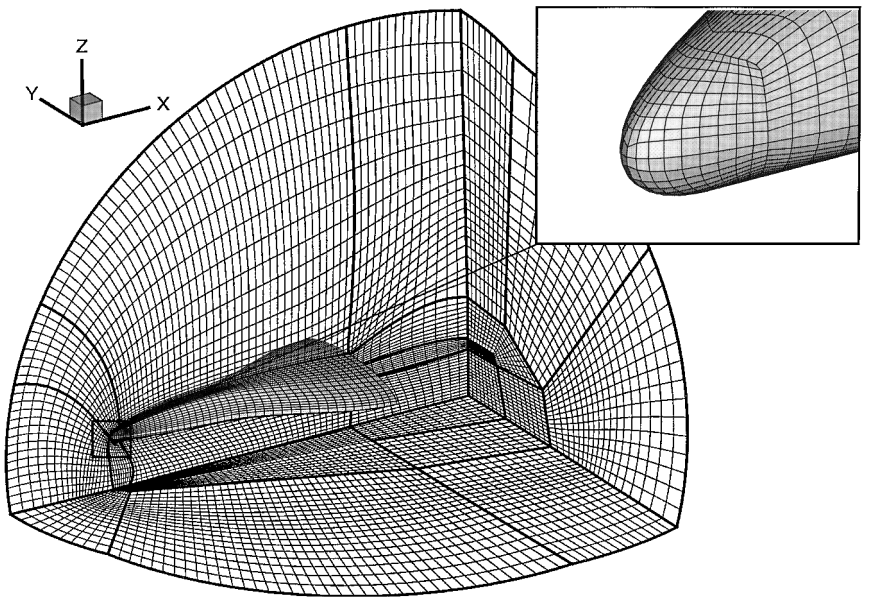

Fig. 2 Computational mesh with C–H topology using 140,000 cells arranged in nine blocks.

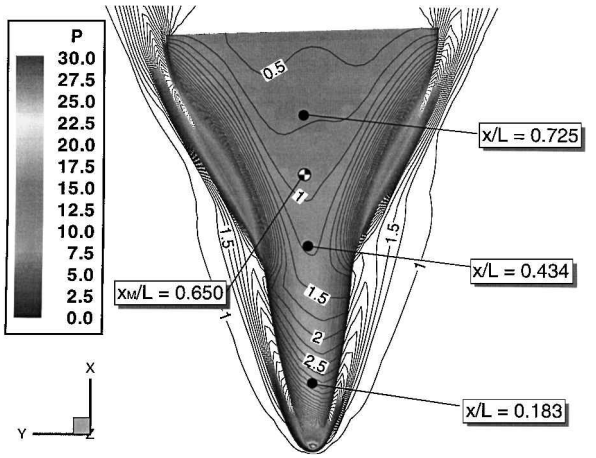

Fig. 3 Contours of constant flowfield and surface pressure at the orbital stage upper side with $\Delta p/p_\infty = 0.5$ for an angle of sideslip of $\beta = 2$ deg at $M_\infty = 6.8$, $\alpha = 0$ deg, $\Phi = 0$ deg, and $h/L = 0.225$.

and $\Phi_0 = 0$ deg with an amplitude of $\Delta\beta = 2$ deg and $\Delta\Phi = 2$ deg, respectively. The results shown herein include flowfield and surface pressure distributions at the orbital stage for steady sideslip and bank angles, as well as side force, roll moment, and yaw moment coefficients for the yaw and roll oscillations.

Steady Angle of Sideslip and Yaw Oscillation

Figure 3 shows contours of constant pressure of the flowfield and the orbital stage upper surface at an angle of sideslip of $\beta = 2$ deg. Because of sideslip, the bow shock is moved to the windward side at the front part of the orbital stage. Therefore, compared to $\beta = 0$ deg, the shock impinging area increases on the windward side while the corresponding area on the leeward side decreases. The region of high pressure on the windward side displaces the low-pressure area to the leeward side. This lateral shift of the shock impinging areas then changes harmonically with the angle of sideslip during the yaw motion.

The steady and unsteady force and moment coefficients arising from the cases with fixed angles of sideslip and the harmonic yaw motions, respectively, are shown in Fig. 4. For better comparison, the steady-state values are plotted as circles. At the beginning of the unsteady motion, a discontinuous change of the airloads occurs. Considering the reduced frequencies employed, there are five cycles required to get fully periodical results. The curves of the unsteady aerodynamic coefficients show a symmetric behavior with respect to the steady-state value of the initial position. Specifically, the side force coefficient C_Y is almost in line with the steady-state values, and thus, the unsteady effect is very small. A positive sideslip angle β results in a negative side force coefficient C_Y and in a negative yaw moment coefficient referred to the moment reference position at $x_M/L = 0.65$. Side force, yaw, and roll moment curves are in the clockwise direction. With regard to the yaw moment and roll moment coefficients, unsteady effects are more obvious than for the side force coefficient C_Y. In particular, the unsteady yaw moment values differ from the steady-state values. The area enclosed by the yaw moment curve is much larger compared to the curve given by the roll moment coefficient. For both reduced frequencies, the main axis of the ellipses nearly coincides with the line given by the steady-state values. The influence of unsteadiness grows with increasing frequency. Hence, the phase shift of the induced airloads increases.

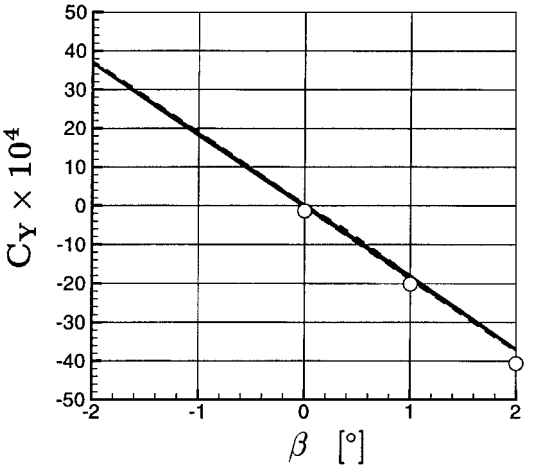

Side force coefficient $C_Y(\beta)$

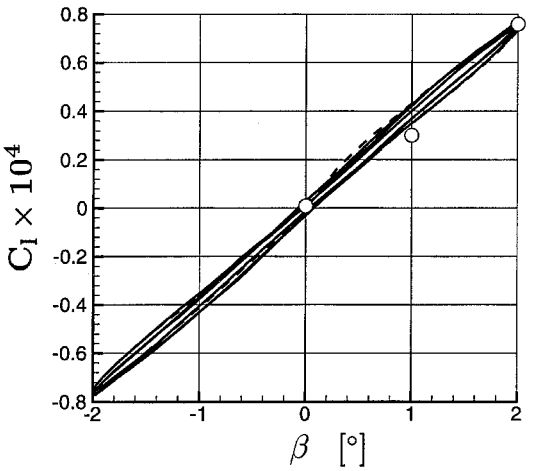

Roll moment coefficient $C_l(\beta)$

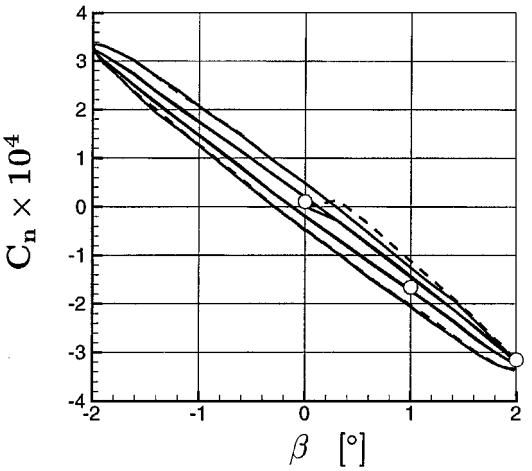

Yaw moment coefficient $C_n(\beta)$

Fig. 4 Steady and unsteady aerodynamic coefficients for the orbital stage at angles of sideslip, $\beta = 0$, 1, and 2 deg, and a harmonic yaw oscillation with mean angle $\beta_0 = 0$ deg, amplitude $\Delta\beta = 2$ deg, and reduced frequencies of $k = 0.1$ and 0.5, at $M_\infty = 6.8$, $\alpha = 0$ deg, $\Phi = 0$ deg, and $h/L = 0.225$: ○, steady values; ——, $k = 0.1$; and – – –, $k = 0.5$.

Steady Angle of Bank and Roll Oscillation

Figure 5 shows pressure contours for the wake region of the orbital stage when the steady state with angle of bank of $\Phi = 2$ deg is considered. Because of the small bank angle, the wake flowfield is nearly symmetric to the midsection of the orbital stage. Recompression shocks are visible around the wing tips.

Figure 6 shows the steady and unsteady force and moment coefficients related to the cases with given angles of bank and the harmonic roll motion, respectively. In general, for the quasi steady state the side force is based on the bank-angle-dependent component of the lift vector. With regard to the flow conditions of the initial position, the negative lift value at zero incidence results in a negative side force component for positive bank angles. However, a roll motion with increasing frequency clearly shows a deviation of the coefficients from the steady-state values and an increase in phase shift. The steady-state values indicate that a negative roll moment is induced by positive bank angles because the pressure on the lower side of the inclined wing tip is higher than the pressure on the

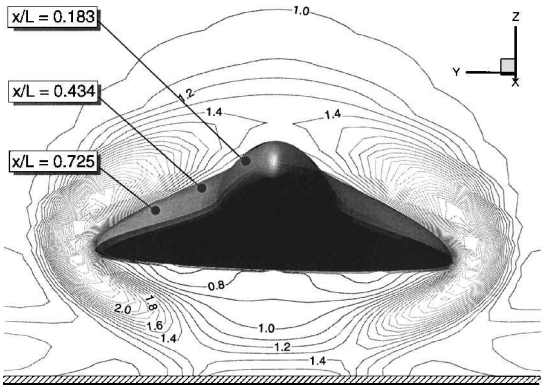

Fig. 5 Contours of constant pressure in a wake plane of the orbital stage with $\Delta p/p_\infty = 0.5$ for an angle of bank of $\Phi = 2$ deg at $M_\infty = 6.8$, $\alpha = 0$ deg, $\beta = 0$ deg, and $h/L = 0.225$.

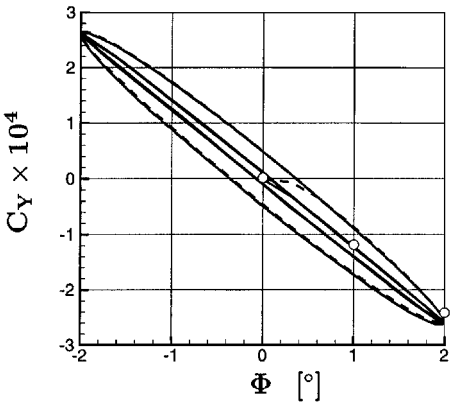

Side force coefficient $C_Y(\Phi)$

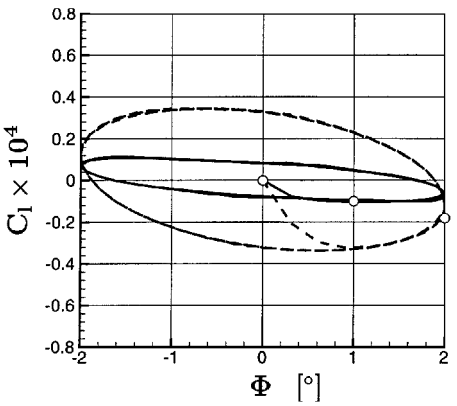

Roll moment coefficient $C_l(\Phi)$

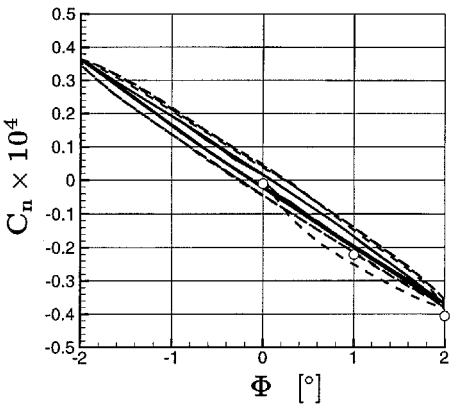

Yaw moment coefficient $C_n(\Phi)$

Fig. 6 Steady and unsteady aerodynamic coefficients for the orbital stage at angles of bank, $\Phi = 0$, 1, and 2 deg, and a harmonic roll oscillation with mean angle $\Phi_0 = 0$ deg, amplitude $\Delta\Phi = 2$ deg, and reduced frequencies of $k = 0.1$ and 0.5, at $M_\infty = 6.8$, $\alpha = 0$ deg, $\beta = 0$ deg, and $h/L = 0.225$: ○, steady values; ——, $k = 0.1$; and – – –, $k = 0.5$.

opposite side. This situation results in a stable rolling behavior of the orbital stage.

The influence of the unsteady motion on the roll moment is such that, due to the roll motion, an additional velocity component is induced, which decreases the negative lift force on the inclined wing tip side. An enforcement of the stable situation is the consequence. The curve of the side force coefficient is in the clockwise direction, whereas the curves of the roll and yaw moment coefficients are characterized by a counterclockwise direction. As found for the yaw motion, the main axis of the ellipses are almost coincident with the lines defined by the steady-state values.

Lateral Flight Dynamics and Stability

Basic Flight Dynamics

For dynamic stability investigations,[19] a hypersonic flight test vehicle with ramjet propulsion was chosen as a reference configuration (HYTEX R–A_3).[20,21] Also, the carrier stage of a parallel-staged winged space transportation system with airbreathing propulsion was used.[5] For aircraft control, maneuvering, and stabilization, these vehicles feature as aerodynamic control surfaces: tailerons (HYTEX), elevons (carrier stage), and rudder (both).

Corresponding to the flight regime with ramjet propulsion systems, the hypersonic flight envelope of both vehicles concerns the same Mach number range up to approximately Mach 7. For the test vehicle, a reference trajectory was specified, consisting of an acceleration phase from $M_\infty \approx 3.5$ (altitude 17.5 km) up to $M_\infty \approx 6.8$ (altitude approximately 30 km), followed by a deceleration part with engine off. A representative set of altitude/Mach number combinations of the test profile was chosen to serve as reference flight conditions for investigating the dynamics and control of the vehicle.

As a basis for the dynamics analysis,[19] a nonlinear six-degree-of-freedom aircraft simulation model was developed with special regard to hypersonic flight effects. Particular emphasis was placed on a realistic modeling of aerothermodynamics and ramjet engine characteristics, including interaction effects. The linearized equations of motion (lateral dynamics) can be expressed in state-space form as

$$\dot{\boldsymbol{x}} = \boldsymbol{A}\boldsymbol{x} + \boldsymbol{B}\boldsymbol{u} + \boldsymbol{E}\boldsymbol{z}, \qquad \boldsymbol{y} = \boldsymbol{C}\boldsymbol{x} + \boldsymbol{D}\boldsymbol{z} \tag{3}$$

The state, control, and disturbance vectors are

$$\boldsymbol{x} = [p, r, \beta_K, \Phi, \Psi]^T, \qquad \boldsymbol{u} = [\xi, \zeta]^T, \qquad z = \beta_W = v_W/V_0$$

The corresponding system, control, and disturbance matrices are given by

$$\boldsymbol{A} = \begin{bmatrix} L_p & L_r & L_\beta & 0 & 0 \\ N_p & N_r & N_\beta & 0 & 0 \\ Y_p & Y_r - 1 & Y_\beta & \dfrac{g}{V_0}\cos\theta_0 & 0 \\ \dfrac{\cos\gamma_0}{\cos\theta_0} & \dfrac{\sin\gamma_0}{\cos\theta_0} & 0 & 0 & 0 \\ \dfrac{\sin\alpha_0}{\cos\theta_0} & \dfrac{\cos\alpha_0}{\cos\theta_0} & 0 & 0 & 0 \end{bmatrix}$$

$$\boldsymbol{B} = \begin{bmatrix} L_\xi & L_\zeta \\ N_\xi & N_\zeta \\ Y_\xi & Y_\zeta \\ 0 & 0 \\ 0 & 0 \end{bmatrix}, \qquad \boldsymbol{E} = \begin{bmatrix} -L_\beta \\ -N_\beta \\ -Y_\beta \\ 0 \\ 0 \end{bmatrix}$$

The output vector together with the corresponding output and direct feed through matrices read

$$\boldsymbol{y} = [p, r, \beta, \Phi]^T, \qquad \boldsymbol{C} = \boldsymbol{I}_{4\times 5}, \qquad \boldsymbol{D} = [0, 0, -1, 0]^T$$

Dynamic and control characteristics of the vehicles are investigated for a c.g. range, the forward limit of which is specified as x_{for}, yielding positive pitch stability for the whole reference trajectory, and the rearward limit as x_{opt}, corresponding to the minimum trimmed drag configuration at a Mach number of $M = 6.8$,

and showing inherent instability.[11] Furthermore, a reference position x_{ref} was chosen as a suitable compromise between these two boundaries, featuring marginal pitch stability up to $M = 5.5$ and slightly aperiodic instability for higher Mach numbers.

Lateral–Directional Dynamics and Stability Characteristics

Unlike the longitudinal motion, where short- and long-term dynamics may be considered separately due to different frequency levels, the lateral motion shows more coupling. Furthermore, there are large changes in the shapes of the lateral modes of motion because they are highly dependent on configuration and flight conditions. Nevertheless, there are usually three modes in subsonic as well as in supersonic and hypersonic flight: the Dutch roll oscillation, the roll subsidence, and the spiral mode.

An evaluation of inherent Dutch roll characteristics of the test vehicle is presented in Fig. 7, and related flying quality requirements are indicated. The upper part of Fig. 7 shows the natural frequency ω_n and the damping coefficient ζ of the forward c.g. configuration for the reference trajectory. Additionally, the corresponding values of the reference c.g. configuration are plotted as dashed lines. Up to $M \approx 6$, the Dutch roll is stable but has a low damping. Beyond Mach 6 (respectively, $M = 6.5$ for the forward c.g. configuration) the Dutch roll is oscillatory unstable with a minimum time to double amplitude $T_D = 46.1$ s. At the rearward c.g. position, x_{opt}, the Dutch roll is unstable and becomes aperiodic above $M = 5.5$ with a minimum time to double, $T_D = 0.38$ s, as shown in the lower part of Fig. 7.

Another flying qualities metric is roll–yaw coupling. As a measure for roll–yaw coupling, the amplitude ratio of bank angle Φ vs sideslip angle β in the Dutch roll oscillation is used. The term $|\Phi/\beta|$ approximately quantifies the roll reaction to a disturbance in sideslip. From the Dutch roll eigenvector relation, the following approximation for roll–yaw coupling can be obtained ($N_\beta > 0$):

$$\left|\frac{\phi}{\beta}\right| \approx \left|\frac{L_\beta}{N_\beta}\right| \approx \left|\frac{C_{l\beta}}{C_{n\beta}}\right| \cdot \frac{I_z}{I_x} \tag{4}$$

Roll–yaw coupling characteristics of the test vehicle are shown in Fig. 8, with reference made to flying requirements.[22] The values of

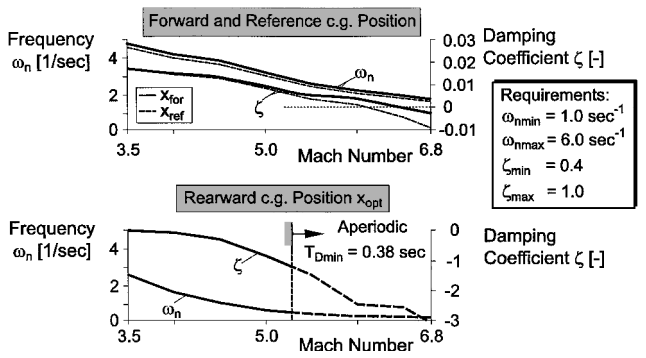

Fig. 7 Inherent Dutch roll stability characteristics of the hypersonic test vehicle configuration (HYTEX R–A_3).

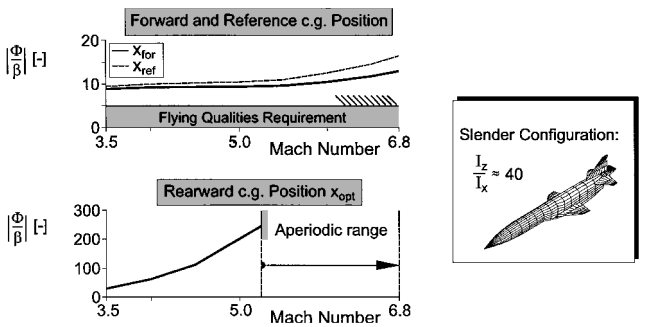

Fig. 8 Roll–yaw coupling $|\Phi/\beta|$ in Dutch roll oscillation of the hypersonic test vehicle configuration.

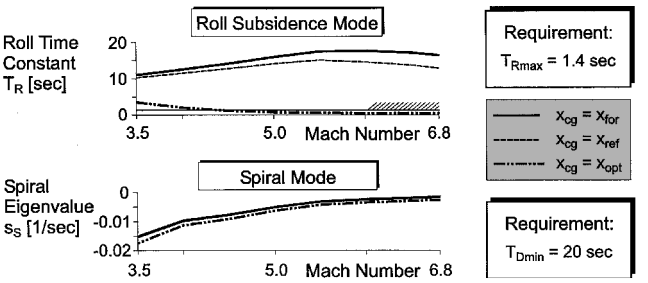

Fig. 9 Inherent stability characteristics of roll subsidence and spiral mode of the hypersonic test vehicle configuration.

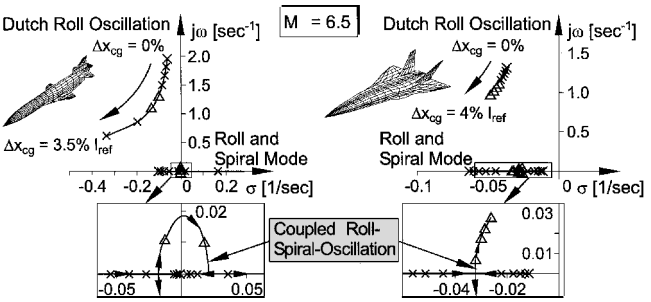

Fig. 10 Effect of a rearward c.g. shift on the lateral–directional dynamics for the hypersonic test vehicle configuration and the carrier stage of a two-staged space transportation system.

$|\Phi/\beta|$ are rather high with a maximum ratio of $|\Phi/\beta| \approx 14$ for the forward and 17 for the reference c.g. positions at $M = 6.8$. For the rearward c.g. position x_{opt}, values of $|\Phi/\beta|$ over 200 are obtained. Because the ratio of $|\Phi/\beta|$ is approximately proportional to the ratio of inertia I_z/I_x according to Eq. (4), a reason for these high values is due to the slender configuration of the test vehicle with a low I_x. Additionally, the decrease in directional stability $C_{n\beta}$ with a rearward c.g. shift causes extremely high values for the c.g. position x_{opt}.

Stability characteristics of the roll subsidence and the spiral mode are presented in Fig. 9, with reference made to flying quality requirements. The upper part of Fig. 9 shows the roll time constant T_R of the three c.g. configurations for the test profile. The roll mode has a weak damping, according to hypersonic aerodynamic characteristics. The spiral mode, shown in the lower part of Fig. 9, is almost neutrally stable and, therefore, meets flying quality requirements that allow a slight spiral instability. Summarizing, inherent lateral stability characteristics of the vehicle in hypersonic flight may present significant flying quality deficiencies because of a weak roll damping in combination with partial Dutch roll instability and high roll–yaw coupling. Moreover, the Dutch roll can also change from an oscillatory into an unstable aperiodic mode.

For certain configurations of hypersonic vehicles, another lateral stability problem occurs. If the roll damping $|C_{lp}|$ is increased to a critical point, the eigenvalues of the roll and the spiral modes start to move toward each other with a rearward shift of the c.g. position. This movement of eigenvalues is shown in Fig. 10 as root loci for the hypersonic test vehicle and for the carrier stage of the two-stage space transportation system (c.g. shift step size 0.5% l_{ref}). Regarding the longitudinal motion, a rearward c.g. shift primarily affects the short-term behavior (due to the change in pitch moment with α) and, in case of sufficient static stability, causes minor effects on the long-term dynamics. By contrast, all modes of the lateral motion are similarly affected by a rearward c.g. shift. Because of the reduced directional stability ($\Delta C_{n\beta} = C_{Y\beta} \cdot \Delta x_{cg}/s_{ref}$), the frequency of the Dutch roll oscillation is decreased with a rearward c.g shift. The roll and spiral eigenvalues move toward each other and combine to yield a slow coupled roll–spiral oscillation, which is called lateral phugoid. Because this oscillatory mode is hard to control and causes problems in lateral maneuvering, it is undesirable and not acceptable for many flight phases.[22] An unstable lateral phugoid, as shown in the left part of Fig. 10, is generally not allowed and has to be avoided. Hence, it is necessary to investigate the reasons for the

appearance of this unusual mode and to investigate how to resolve this stability problem by adequate means, for example, configuration modifications and/or feedback control.

Approximations and Analysis of Lateral–Directional Dynamics

To gain better physical insight into the complex properties of lateral dynamics, it is useful to investigate the different modes by appropriate approximations. Because hypersonic dynamics characteristics show significant differences when compared with relations in subsonic and moderate supersonic flight, specific approximations are needed. The proposed approach to determine suitable approximations for the hypersonic flight regime is based on the characteristic determinant of the fourth-order state-space equations (with the decoupled heading Ψ equation canceled out):

$$N(s) = \det(s\boldsymbol{I} - \boldsymbol{A}') = s^4 + a_3 s^3 + a_2 s^2 + a_1 s + a_0$$
$$= \left[s^2 - 2\sigma_d s + \omega_{nd}^2\right]\left[s^2 - (s_s + s_r)s + s_s s_r\right] \quad (5)$$

With regard to the magnitude of the Dutch roll and the roll/spiral poles, it can be assumed that $|s_d| \gg |s_{s,r}|$ in the Mach number regime of interest (Figs. 7, 9, and 10). Therefore, a second-order polynomial concerning the spiral and roll poles can be separated from the fourth-order characteristic determinant. After neglecting less important terms, an approximation for the roll and spiral modes results, also holding for coupling of the two poles to form the lateral phugoid:

$$2s_{s,r} \approx L_p + (g/V_0 - N_p)(L_\beta/N_\beta)$$
$$\pm\sqrt{[L_p + (g/V_0 - N_p)(L_\beta/N_\beta)]^2 - 4N_r(g/V_0)(L_\beta/N_\beta)} \quad (6)$$

Splitting off the roll–spiral approximation [Eq. (6)] from the complete characteristic polynomial yields the following relations for the Dutch roll oscillation:

$$\omega_{nd} \approx \sqrt{N_\beta}$$
$$2\sigma_d \approx N_r + Y_\beta - (g/V_0 - N_p)(L_\beta/N_\beta) \quad (7)$$

In Fig. 11, an evaluation of the approximations is shown together with the exact solutions of the fourth-order polynomial for the hypersonic test vehicle. Instead of varying the c.g. position, the weathercock stability $C_{n\beta}$ is changed because this step yields the same effect as shown before. The approximation results are consistent with the exact solutions, especially with regard to the coupled roll–spiral oscillation. Comparable accurate results are obtained for the carrier and orbital stages of the space transportation system in the Mach number range of concern.

The natural frequency ω_{nd} of the Dutch roll oscillation is primarily determined by N_β, analogous to the conditions of subsonic and supersonic flight. The damping exponent σ_d includes several contributions. Particularly, a term that is related to roll–yaw coupling is of importance:

$$(g/V_0 - N_p)|L_\beta/N_\beta| \approx (g/V_0 - N_p)|\Phi/\beta| \quad (8)$$

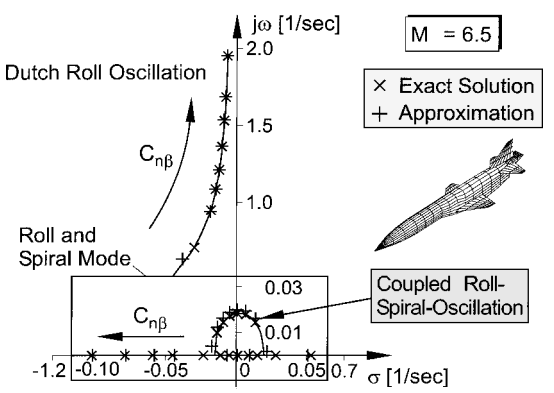

Fig. 11 Approximations and exact solutions of lateral flight dynamics for the hypersonic test vehicle configuration.

This expression may show a positive or negative sign, depending on the configuration or flight condition. The second-order approximation for the spiral and roll modes basically differs from the usual first-order approximations valid in subsonic flight. Because of the small aerodynamic damping in hypersonic flight, the stability derivatives L_p and N_r are less important, and the terms of Eq. (8) are of significance. From Eq. (6), it follows that the coupled roll–spiral oscillation exists for

$$[L_p + (g/V_0 - N_p)(L_\beta/N_\beta)^2] < 4N_r(g/V_0)(L_\beta/N_\beta) \quad (9)$$

From this relation, conditions can be derived, indicating a possible existence of the lateral phugoid:

1) $L_\beta/N_\beta < 0$ is necessary for Eq. (9) because $N_r < 0$.

2) For $(g/V_0 - N_p) < 0$, the two summands in the parenthesis on the left-hand side are opposed to each other.

3) Because of $|\Phi/\beta| \approx |L_\beta/N_\beta|$, there is a high roll–yaw coupling for small $|g/V_0 - N_p|$.

For developing a criterion for the existence of the lateral phugoid, Eq. (9) may be rewritten as

$$(L_p + b \cdot \nu)^2 < c \cdot \nu \quad (10)$$

with

$$b = (g_0/V_0 - N_p), \qquad c = -4N_r(g_0/V_0)$$

The substitution $\nu = -L_\beta/N_\beta \approx |\Phi/\beta|$ can be used as a measure for roll–yaw coupling, with $\nu \geq 0$ (assuming $N_\beta > 0$ and $L_\beta \leq 0$). For the quantity c, the relation $c \geq 0$ holds because the damping derivatives L_p and N_r are negative. The factor b may be positive or negative. After considering the different cases, a condition for the existence of the lateral phugoid can be derived:

$$N_p > (g_0/V_0)(1 - N_r/L_p) \quad (11)$$

This relation, which is based on the second-order approximation, holds for the special case where $N_p = g_0/V_0$. It can be used to show whether or not the lateral phugoid exists. As long as the condition

$$N_p\,(V_0/g_0) + N_r/L_p > 1 \quad (12)$$

holds, it is assured that the lateral phugoid will not appear within the scope of approximations given earlier. If the condition is violated, the coupled roll–spiral oscillation will exist within a roll–yaw coupling range of $\nu_{\min} < \nu = |\Phi/\beta| < \nu_{\max}$, where $\nu_{\min}$ and $\nu_{\max}$ are given as the two positive zeros of

$$b^2\nu^2 + (2bL_p - c)\,\nu + L_p^2 = 0 \qquad \forall\ b \neq 0 \quad (13)$$

An evaluation of this criterion is shown in Fig. 12 for the experimental vehicle (reference flight condition $M = 6.5$). If C_{nr} and C_{np} are considered as fixed, a critical value $(C_{lp})_{\text{crit}}$ can be determined

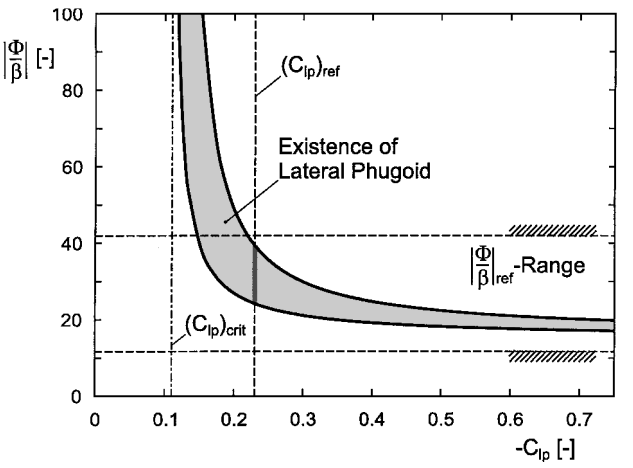

Fig. 12 Range of existence of the lateral phugoid, computed for the hypersonic test vehicle configuration at $M_\infty = 6.5$.

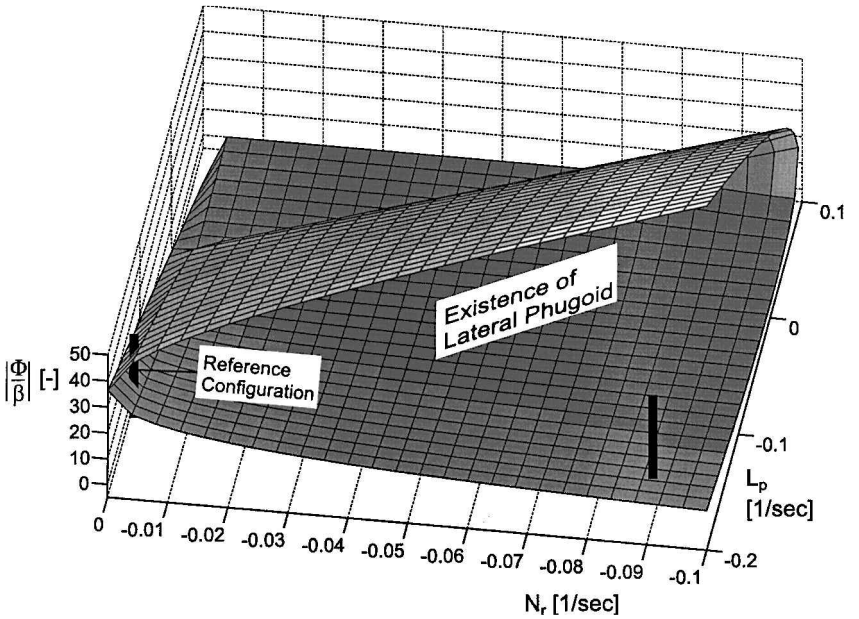

Fig. 13 Boundary surfaces for existence of the lateral phugoid, evaluated for the hypersonic test vehicle configuration at $M_\infty = 6.5$.

for the existence of lateral phugoid according to Eq. (12). In case of $|C_{lp}| \geq (C_{lp})_{\text{crit}}$, a $|\Phi/\beta|$ region exists, which is bounded by the positive zeros of Eq. (13), with $(C_{lp})_{\text{crit}}$ as left asymptote.

An extension of the described approach for multivariable parameters is shown in Fig. 13. As an example, the surface of $|\Phi/\beta|$ corresponding to a variation of the stability derivatives L_p and N_r is plotted for the reference flight condition with $M = 6.5$. Additionally, the ranges of $|\Phi/\beta|$ are marked by bars for the configuration associated to the root loci of Fig. 11 and for a configuration with a higher L_p and N_r. Considering a rearward c.g. shift, Fig. 13 shows that the values of roll–yaw coupling are initially beneath the lower surface. Then, they are above the lower surface indicating that there is a lateral phugoid. When they are above the upper surface, there are again two aperiodic modes of motion. Figure 13 also shows that the configuration with higher damping values shows a lateral phugoid for the whole $|\Phi/\beta|$ reference range. The condition described by Eq. (12), in combination with Eq. (13), offers the possibility of avoiding critical combinations of stability derivatives by concerning the lateral phugoid in a preliminary design phase of the vehicle and/or the control system. Hence, this specific stability problem in hypersonic flight can be counteracted effectively, for example, by choosing appropriate feedback control paths and gains.

Summarizing the results of the investigations, a high roll–yaw coupling in combination with weak aerodynamic damping can be a main reason for the stability deficiencies of lateral dynamics in hypersonic flight. By the specification of an appropriate criterion concerning the lateral phugoid, critical configurations of aerodynamic and/or controller coefficients may be identified in an early design phase. Subsequently, suitable modifications and requirements with regard to configuration and controller design can be elaborated.

Conclusions

Unsteady aerodynamic effects and lateral dynamic stability characteristics in hypersonic flight up to a Mach number of 7 are discussed for a two-staged space transportation system and a hypersonic test vehicle as reference configurations. The aerodynamic investigations focus on harmonic yaw and roll motions of a generic orbital stage induced by small disturbances during separation from the carrier stage. The associated unsteady flowfields are calculated using a finite volume method to solve the three-dimensional Euler equations. The numerical fluxes are treated with the modified AUSM method featuring robustness and stability, especially in low-density wake regions. Flowfield and surface pressure distributions, as well as lateral aerodynamic coefficients, are evaluated. For both the yaw and roll motions, the unsteady moment coefficients differ from the steady-state values, whereas the magnitude of the unsteadiness depends on the reduced oscillation frequencies. It substantiates the need for time-accurate aerodynamic solutions to evaluate stability derivatives to simulate correctly the separation maneuver. Further, inherent lateral–directional dynamics of hypersonic vehicles show considerable stability and control deficiencies. In addition to a partially unstable Dutch roll mode with high roll–yaw coupling and a weak roll damping, coupling of the roll and spiral modes appears for certain configurations to yield an oscillatory mode called lateral phugoid. The lateral phugoid can cause significant control problems and may be unstable. By use of specific approximations, reasons for the stability deficiencies and related effects are analyzed, and a criterion concerning the existence of the lateral phugoid is derived.

Acknowledgment

The subject of this paper is part of the research work undertaken in the Collaborative Research Center 255 "Transatmospheric Flight Systems—Fundamentals of Aerothermodynamics, Powerplants and Flight Mechanics" of the German Research Association (Deutsche Forschungsgemeinschaft) at the Technical University of Munich.

References

[1] Kuczera, H., Sacher, P. W., and Dujarric, C., "FESTIP System Study—An Overview," AIAA 7th International Space Planes and Hypersonic Systems and Technologies Conf., Nov. 1996.

[2] Falempin, F., Scherrer, D., Laruelle, G., Rostand, P., Hermant, E., and Dubois, I., "French Hypersonic Propulsion Program PREPHA: Results, Lessons and Perspectives," AIAA Paper 98-1565, April 1998.

[3] Maita, M., and Kubota, H., "Japanese Spaceplane/RLV Program," AIAA 8th International Aerospace Planes and Hypersonic Systems and Technologies Conf., April 1998.

[4] Sancho, M., "The French Hypersonic Research Program: Progress Review," AIAA Paper 95-6004, April 1995.

[5] Kania, P., "The German Hypersonics Technology Program—Overview," AIAA Paper 95-6005, April 1995.

[6] Freeman, D., Reubusch, D., McClinton, C., Rausch, V., and Crawford, L., "The NASA Hyper–X Program," International Astronautical Federation, Rept. IAF-97-V.4.07, Oct. 1997.

[7] Weiland, C., "Stage Separation Aerodynamics," *Aerothermodynamics and Propulsion Integration for Hypersonic Vehicles*, R-813, AGARD, Oct. 1996, pp. 11-1–11-28.

[8] Rochholz, H., "Euler Solutions for the Separation of Carrier/Orbiter Systems in Hypersonic Flow," Dissertation, Technical Univ. of Munich, Aug. 1994 (in German).

[9] Rochholz, H., Huber, T., and Matyas, F., "Unsteady Airloads During the Separation of an Idealized Two-Stage Hypersonic Vehicle," *Zeitschrift für Flugwissenschaften und Weltraumforschung*, Vol. 19, No. 1, 1995, pp. 2–9.

[10]Cvrlje, T., Breitsamter, C., Heller, M., and Sachs, G., "Unsteady Aerodynamics and Dynamic Stability of Hypersonic Vehicles," German Aerospace Congress/German Aerospace Society Meeting, Rept. DGLR-JT98-207, Oct. 1998, pp. 89–102 (in German).

[11]Sachs, G., Heller, M., and Wahlberg, L., "Robust Control of a Hypersonic Experimental Vehicle with Ramjet Engines," AIAA Paper 96-3728, July 1996.

[12]Sachs, G., "Flight Qualities Criteria and Long Term Dynamics in Supersonic and Hypersonic Flight," *Zeitschrift für Flugwissenschaften und Weltraumforschung*, Vol. 15, No. 4, 1991, pp. 243–251 (in German).

[13]Radespiel, R., and Kroll, N., "Accurate Flux Vector Splitting for Shocks and Shear Layers," *Journal of Computational Physics*, Vol. 121, 1995, pp. 66–79.

[14]Cvrlje, T., Breitsamter, C., and Laschka, B., "Numerical Simulation of the Lateral Aerodynamics of an Orbital Stage at Stage Separation Flow Conditions," *Aerospace Science and Technology*, Vol. 4, No. 3, 2000, pp. 157–171.

[15]Liou, M. S., "On a New Class of Flux Splittings," *Lecture Notes in Physics*, Vol. 414, 1992, pp. 115–119.

[16]Liou, M. S., and Steffen, C., "A New Flux Splitting Scheme," *Journal of Computational Physics*, Vol. 107, 1993, pp. 23–39.

[17]Cvrlje, T., Breitsamter, C., and Laschka, B., "Unsteady Hypersonic Flows," Collaborative Research Center 255, Work and Result Rept. June 1995–June 1998, Technical Univ. of Munich, Munich, May 1998, pp. 21–89 (in German).

[18]Cvrlje, T., Breitsamter, C., Weishäupl, C., and Laschka, B., "Euler and Navier–Stokes Solutions of Two-Stage Hypersonic Vehicle Longitudinal Motions," *Journal of Spacecraft and Rockets*, Vol. 37, No. 2, 2000, pp. 242–251.

[19]Etkin, B., *Dynamics of Atmospheric Flight*, Wiley, New York, 1972, pp. 121–189.

[20]Sacher, P. W., "Flight Testing Vehicles for Verification and Validation of Hypersonics Technology," *Space Systems Design and Development Testing*, FVP, AGARD, Oct. 1994.

[21]Sacher, P. W., and Zellner, B., "Flight Testing Objectives for Small Hypersonic Flight Test Vehicles Featuring a Ramjet Engine," AIAA Paper 95-6014, April 1995.

[22]Military Specification—Flying Qualities of Piloted Airplanes, MIL–F–8785C, MIL Standard and Handbook, Washington, DC, Sept. 1991.

D. B. Spencer
Associate Editor